

All-dielectric one-dimensional gratings exhibiting Fano resonances in the terahertz region

Westerkam, Anders M.; Sonne, Jesper L.W.; Danielsen, Karl G.; Skovsen, Esben; Søndergaard, Thomas M.

Published in:
Journal of the Optical Society of America B: Optical Physics

DOI (link to publication from Publisher):
[10.1364/JOSAB.462062](https://doi.org/10.1364/JOSAB.462062)

Publication date:
2022

Document Version
Accepted author manuscript, peer reviewed version

[Link to publication from Aalborg University](#)

Citation for published version (APA):
Westerkam, A. M., Sonne, J. L. W., Danielsen, K. G., Skovsen, E., & Søndergaard, T. M. (2022). All-dielectric one-dimensional gratings exhibiting Fano resonances in the terahertz region. *Journal of the Optical Society of America B: Optical Physics*, 39(7), 1723-1729. <https://doi.org/10.1364/JOSAB.462062>

General rights

Copyright and moral rights for the publications made accessible in the public portal are retained by the authors and/or other copyright owners and it is a condition of accessing publications that users recognise and abide by the legal requirements associated with these rights.

- Users may download and print one copy of any publication from the public portal for the purpose of private study or research.
- You may not further distribute the material or use it for any profit-making activity or commercial gain
- You may freely distribute the URL identifying the publication in the public portal -

Take down policy

If you believe that this document breaches copyright please contact us at vbn@aub.aau.dk providing details, and we will remove access to the work immediately and investigate your claim.

All-dielectric one-dimensional gratings exhibiting Fano resonances in the terahertz region

ANDERS M. WESTERKAM,¹ JESPER L. W. SONNE,¹ KARL G. DANIELSEN,¹ ESSEN SKOVSEN,¹ AND THOMAS M. SØNDERGAARD^{1,*}

¹Department of Materials and Production, Aalborg University, DK-9220 Aalborg Øst, Denmark

*ts@mp.aau.dk

Abstract: Transmittance spectra of an all-dielectric sub-wavelength grating exhibiting Fano resonances are studied both experimentally and theoretically for a frequency interval spanning several terahertz using both S- and P-polarized radiation. Modelled spectra based on the Rigorous Coupled Wave Analysis are shown to be in good agreement with the Fourier transform of measured time-domain transmission spectra for normal and angled incidence. Finally, a model is presented that explains Fano resonance frequencies by matching the propagation constant of a discrete set of guided modes to wave-numbers that both match diffraction orders in the grating and are in a range that allows propagation in the dielectric medium.

© 2023 Optica Publishing Group

1. Introduction

The application of terahertz (THz) radiation has shown promising results in numerous fields, e.g., spectroscopy and imaging which can be utilised in the public safety and defense sector [1,2], as non-destructive quality control [3–6], medical diagnostics [3, 7, 8], and research in biochemistry [8, 9]. Furthermore, it is proposed that the THz region will be fundamental for the next generation of telecommunication since following the current trend of the technology it is expected that the 6G-bands will extend into the THz region [10–12].

Many of the components commonly used to manipulate optical and microwave radiation are not readily available in the THz range [13], thus components such as optical filters, switches, and reflectors [14, 15] enabling the manipulation of THz waves are of interest [12]. These components would, depending on the application, benefit from having high quality-factors (Q-factors), making them very frequency selective [14, 15].

A phenomenon which can be exploited to achieve high Q-factors is Fano resonances [14–19]. They are well established in the literature [15–22], first described by Fano as a means to explain the asymmetric spectra from helium atoms subjected to inelastic scattering from electrons [23]. Fano resonances occur when a discrete and continuous set of states are available at the same time resulting in an asymmetric spectral line-shape, known as a Fano resonance. These resonances may exhibit complete destructive interference that can be exploited to achieve zero transmission at certain frequencies [15, 23, 24].

In the literature Fano resonances have been found for a multitude of different structures, or metamaterials (MMs) [21]. The complexity in the designs of the MMs ranges from one-dimensional gratings and structures such as split-ring resonators, to more intricate three-dimensional structures [12, 14, 16, 17, 19, 20, 22]. Furthermore, the Fano resonances of the MMs have in different studies been shown to be highly tunable, hence enabling the possibility to tailor the MMs depending on the task [14, 17, 19–21, 25]. Sub-wavelength structures exploiting Fano resonances has been used for devices such as high-Q-factor optical filters [26, 27] and single-material high-reflectivity mirrors [28].

We present here an all-dielectric structure consisting of a sub-wavelength one-dimensional grating etched in a thin high-resistivity silicon wafer. The wafer was obtained from *SILICON MATERIALS, INC.* with a thickness of $100 \pm 20 \mu\text{m}$, and a resistivity of $\rho > 5000 \Omega\cdot\text{cm}$. Similar

structures have been reported earlier in [14,25], and for other frequency ranges [29–31]. However, we present exceptional agreement between experimentally and theoretically obtained data over a broad frequency range in the THz region. The agreement is shown to hold for both normal and angled incidence, and for both polarisations. The transmittance spectrum of the structure was calculated using the rigorous coupled wave analysis, also known as the Fourier Modal Method (FMM) [32].

Furthermore, a novel model for predicting the existence and center frequencies of Fano resonances in structures similar to the structure presented here is proposed and validated numerically. The advantages of this model are that it gives an intuitive understanding of the underlying physical mechanisms, and that the prediction is done at a low computational cost.

2. Method

The fabricated structure and a schematic of the design are seen in Fig. 1(a). The structure is fabricated using standard photolithography procedures and reactive ion etching (RIE) [33–36], and has the following dimensions: Strip height, $t = 12.9 \mu\text{m}$, period, $\Lambda = 99.7 \mu\text{m}$, strip width $w_t = 32.5 \mu\text{m}$ and wafer thickness, $h = 105 \mu\text{m}$ (Fig. 1). The RIE procedure produces sidewalls with slopes $\Phi = 55^\circ$, with respect to the base of the strip. In the FMM the refractive index of silicon is set to $\varepsilon = 3.4^2$, and the structure is divided into layers in which the permittivity profile is layerwise constant in the z -direction. Thus the sloping sidewalls can in the FMM either be accounted for by performing an area preserving averaging resulting in $w_{t,avg} = 41.5 \mu\text{m}$, or by adding layers to the FMM model and gradually widening the strip width at the top, $w_t = 32.5 \mu\text{m}$, towards the base width, $w_{t,base} = 50.5 \mu\text{m}$ (Fig. 1(b)) [32]. In Fig. 1(c) the FMM model is plotted for S-polarised light using the averaged strip width, and for strips discretised with three to seven steps. It is clear that there is no significant difference between the approaches, why the averaged strip method is used for further spectra.

The time-domain spectrometer (TDS), a *TeraSmart, Compact THz-TDS* from *Menlo Systems* using a scan range of 420 picoseconds, giving a spectral resolution of $> 2.4 \text{ GHz}$, is used to measure time-domain transmittance spectra. Detailed descriptions of the optical and nitrogen purge setup can be found in Ref. [37]. The sample is placed at the collimated part of the beam using an alumina sample holder to block any part of the beam not passing through a 45° tapered circular hole with a minimum diameter of 13 mm in the holder where the sample is placed (Fig. 2). The area of the grated region is $\sim 280 \text{ mm}^2$, while the area of the tapered hole is $\sim 133 \text{ mm}^2$, and consequently the beam does not hit the sample outside of the micro-structured region. The holder can have angles up to 10° without letting any radiation bypass the tapered hole. Fourier transforms are performed in accordance with the method outlined in Ref. [38].

3. Measurements

Fig. 3 shows the measured and modelled transmittance spectra for both polarisations, which are seen to be in good agreement, e.g., the first three measured resonances for both polarisations are found within 9 GHz or less than what is predicted by the model. Furthermore, all measured resonances are also present in the modelled spectra, though there are a few very narrow resonances predicted by the model which are hardly or not visible at all in the measurement, e.g., at 1.82 THz for P-polarisation (\mathbf{H} along $\hat{\mathbf{y}}$) and at 1.94 THz for S-polarisation (\mathbf{E} along $\hat{\mathbf{y}}$). This may in part be due to the finite resolution of the spectrometer. Additionally, the FMM predicts that Fano resonances shift on the order of hundreds of MHz when parameters such as Λ and w_t change by tenths of micrometers, which is approximately the fabrication uncertainty for these parameters. Thus the very narrow resonances could simply be smeared out due to structure variations.

Fano resonances for S-polarised light at 1.40 and 1.73 THz, have a width at 50%-transmittance of 43 and 74 GHz, respectively. This corresponds to Q-factors of 32.55 and 23.38, hence both

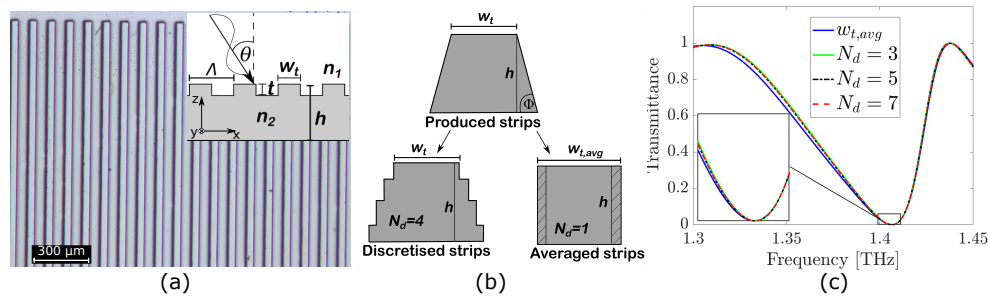


Fig. 1. (a) Light-microscopy image of the fabricated sample and an insert of the modelled structure. Structure parameters: Strip height, $t = 12.9 \mu\text{m}$, period, $\Lambda = 99.7 \mu\text{m}$, strip width $w_t = 32.5 \mu\text{m}$ and wafer thickness, $h = 105 \mu\text{m}$ (b) Cross-section sketch of the produced, discretised and averaged strips. (c) FMM model using the averaged and discretised strips with 3 to 7 discretisations.

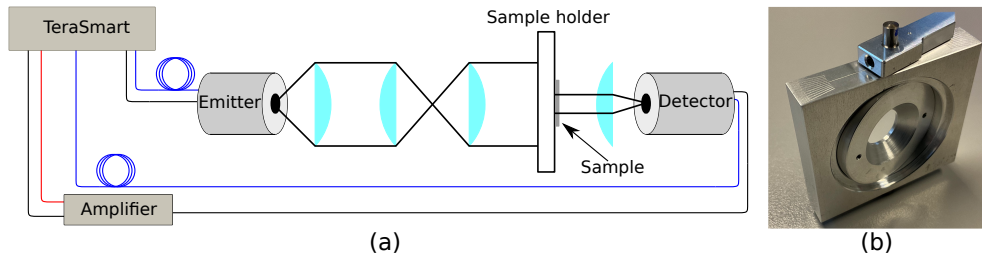


Fig. 2. (a) Schematic of the experimental setup. (b) Image of the front side of the sample holder, in which the taper can be seen.

resonances exceed the Q-factor measured for a similar structure shown in Ref. [25]. The upper frequency limit, considered in Fig. 3, is determined by the spectrometer signal-to-noise ratio.

To further test the correspondence between model and measurements, the angle of incidence is varied between 0° and 10° in steps of 1° , the result of which is presented in Fig. 4. The correspondence between model and measurement are for most resonances striking, both with regards to frequency position and broadness. Only the sharpest resonances in the model are hard to see in the measurements, e.g., the one seen at $\sim 1.8 \text{ THz}$ for the P-polarisation, which is barely visible between 0° and 2° but then fades.

It can be seen that many resonances at $\theta = 0^\circ$ splits into two resonances, which move in opposite directions as the angle of incidence is increased. Using the clearest five resonances for each polarisation, the average change of the Fano resonances between $\theta = 0^\circ$ and 10° is tabulated in Table 1, showing that on average, the change in center frequency of a resonance predicted by the model is within 8 GHz of the measured change, which is the same uncertainty observed between model and measurements at normal incidence. The table also shows that for the sample presented here, the frequency with the lowest transmittance in the resonance can be tuned on the order of tens of GHz simply by changing the angle of incidence. The angle which has to be changed is shown in Fig. 1(a), corresponding to a rotation around the y-axis. Rotating around the x-axis does not appreciably change the spectra, this fact is also reported in [25]. Thus the structure can be used as a spectral specific mirror for a large set of incidence angles.

The discrepancy between the change seen in the measurements and the FMM model for all angles of incidence can be attributed to two factors. The first is that the spectral resolution of the model is much higher than the measurements, making it easier to determine the center frequency

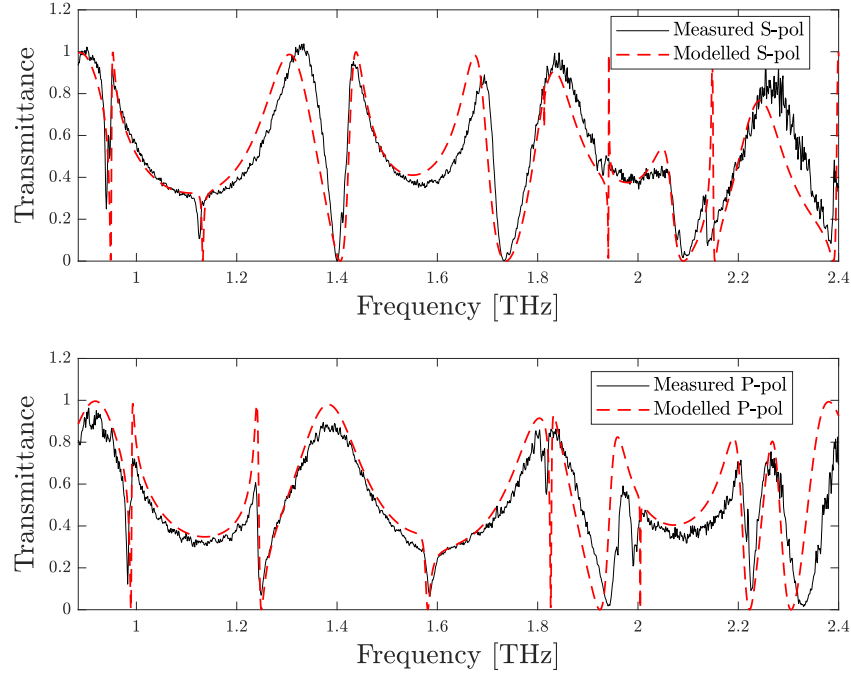


Fig. 3. Fourier transformed time-domain measurements and the transmittance found using the FMM model. The FMM settings were $t = 12.89\mu\text{m}$, $\Lambda = 99.74\mu\text{m}$, $w_t = 41.5\mu\text{m}$, $h = 105\mu\text{m}$, and spectral resolution of 0.42 GHz

of the resonance, and secondly because the angle of incidence on the measured spectra has an uncertainty of $\pm 0.25^\circ$.

	Increase [GHz]	Decrease [GHz]
$\Delta\nu_{S,measured}$	63.3	47.3
$\Delta\nu_{S,modelled}$	65.2	55.2
$\Delta\nu_{P,measured}$	55.5	47.5
$\Delta\nu_{P,modelled}$	60.9	51.4

Table 1. Lists the average increase and decrease of the center frequency of five Fano resonances found using the FMM model and the measured spectra when the angle of incidence is changed from $\theta = 0^\circ$ to $\theta = 10^\circ$.

4. One-dimensional propagation constant matching model

The rigorous FMM model clearly predicts the center frequency of the Fano resonances with high accuracy. However, it is a 2D model which is somewhat computationally expensive, and as such it does not lend itself well to the design of structures with Fano resonances at select frequencies. Furthermore, the FMM does not provide an intuition as to what is causing the Fano resonances, an insight that may further improve the ability to exploit the phenomenon in optical devices.

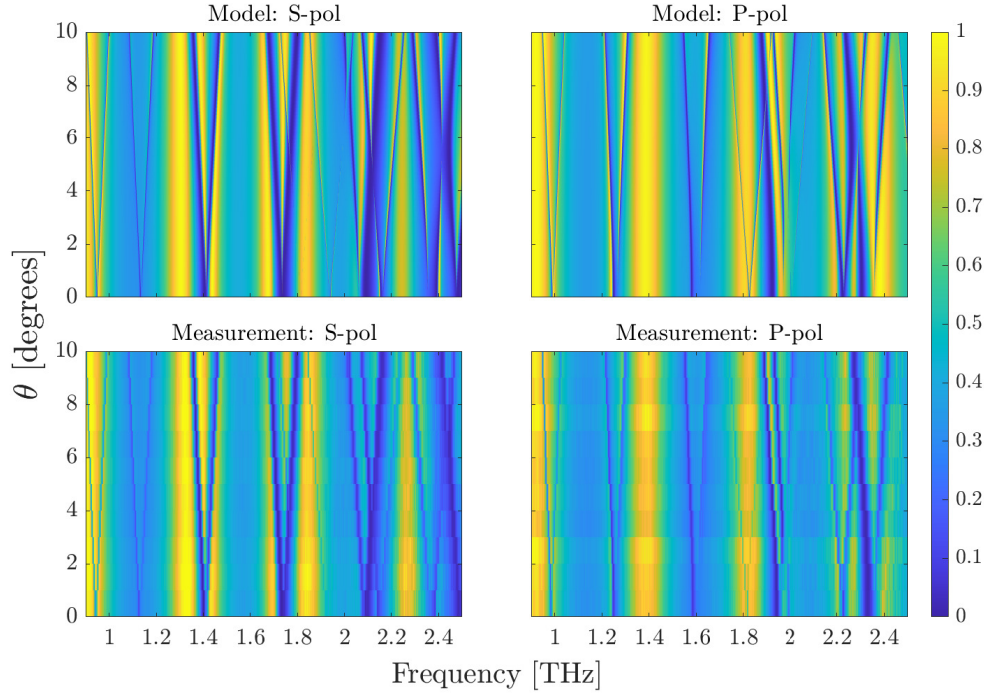


Fig. 4. The Fourier transformed time-domain measurements and the transmittance found using the FMM model for both polarisations with angles of incidence between zero and ten degrees.

Here, we present a novel one-dimensional propagation constant matching model (PMM), which solves both issues.

Assume an incident field on the form of Eq. 1,

$$\mathbf{A} = A_0 e^{-ik_z z} e^{ik_x x} \hat{\mathbf{y}}, \quad (1)$$

with \mathbf{A} denoting either an electric or magnetic field based on the polarisation of interest. The orientation of the field in relation to the structure can be identified from Fig. 5. According to the Helmholtz equation for regions of homogeneous dielectric constant, ϵ_i , the wave-vector component perpendicular to the surfaces is given as

$$k_z = \sqrt{k_0^2 \epsilon_i - k_x^2}. \quad (2)$$

If the structured layer is then viewed as a one-dimensional photonic crystal the resulting in-plane components of the wave vector has to satisfy Bloch's theorem as [39]

$$k_{x,m} = k_x + \frac{2\pi}{\Lambda} m, \quad m = 0, \pm 1, \pm 2, \pm 3, \dots \quad (3)$$

When the in-plane component of a resulting wave vector matches the propagation constant of a quasi-bound mode, it is possible to excite the mode in question. This is the core of the PMM. In other words there are both a discrete and a continuous set for the light to couple to, and hence Fano resonances are possible. In this context the discrete set is the bound modes accessed by the diffracted light and the continuous set is the otherwise reflected and transmitted light.

In the following discussion we limit ourselves to the case $k_x = 0$, though the method does, in theory, work for any angle of incidence. By inspecting Eq. 2 and Eq. 3 limits for the existence of Fano resonances can be extracted. When $k_0 n_{\text{Si}} < \frac{2\pi}{\Lambda}$ propagating solutions with a non-zero \mathbf{k} projection along $\hat{\mathbf{x}}$ does not exist in any regions and hence coupling to the discrete set of bound modes is impossible. This presents a hard boundary for when Fano resonances can occur, and they are indeed not observed for frequencies below this limit in the case of the structure presented in this article. Furthermore, a soft boundary can be introduced by requiring that no propagating diffraction orders exist in the air regions. The frequency region of interest would then be $\frac{c}{\Lambda n_{\text{Si}}} < \nu < \frac{c}{\Lambda}$, corresponding to $0.88 < \nu < 3.01$ THz for the structure presented in Fig. 1(a).

To calculate the propagation constants of quasi-bound modes a one-dimensional finite element method (FEM) for a slab waveguide is employed. In this model bound solutions on the form

$$\mathbf{f}(x, z) = f(z)e^{i\beta_n x}\hat{\mathbf{y}}, \quad (4)$$

are sought after. In Eq. 4 $f(z)$ denotes the field distribution along z and β_n is the propagation constant along $\hat{\mathbf{x}}$ with the subscript n denoting the mode number. It is this propagation constant which is matched with the diffraction orders to predict the center frequency of the Fano resonances. For normal incidence a Fano resonance is then expected whenever Eq. 5 is satisfied:

$$\beta_n = \frac{2\pi}{\Lambda}m. \quad (5)$$

In the FEM model the dielectric constant of the photonic crystal layer is approximated by an effective dielectric constant calculated as the geometric average within a unit cell. Using the

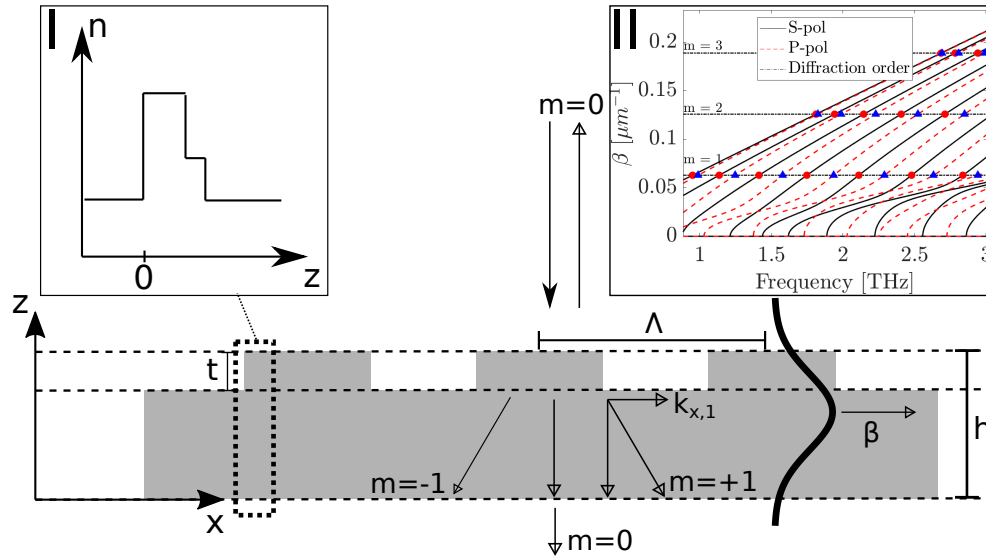


Fig. 5. Sketch of the structure and the diffraction orders for reflected and transmitted light. Insert I: Sketch of the effective-refractive-index in the one-dimensional slab waveguide. Insert II: Matching of the propagation constant with the diffraction orders. Circles: S-polarisation. Triangles: P-polarisation.

geometric average for the dielectric constant does naturally neglect some effects, namely that high-frequency radiation tends to accumulate in the high-refractive-index regions and hence the effective refractive index is expected to increase for higher frequencies [39]. Furthermore, the

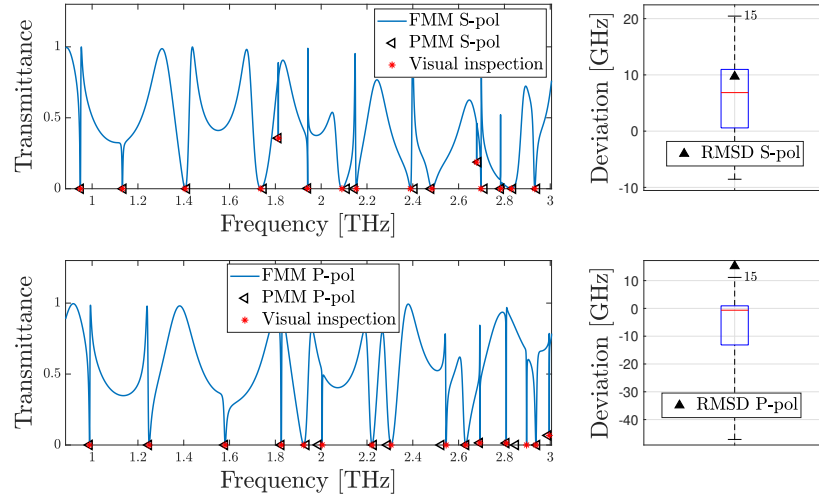


Fig. 6. Comparison of the PMM predictions and visual inspection of the FMM spectra for the fabricated structure studied in this article. The FMM settings were $t = 12.89\mu\text{m}$, $\Lambda = 99.74\mu\text{m}$, $w_t = 41.5\mu\text{m}$, $h = 105\mu\text{m}$, and the calculation had a spectral resolution of 0.1 GHz. The graphs to the left show the spectra calculated with FMM, overlaid with the PMM predictions for the center frequencies. The graphs to the right are box plots of the deviation between the PMM predictions and the visual inspection. Tilted triangles: PMM predictions of Fano center frequencies. Asterisks: Fano center frequencies found from visual inspection of the spectra. Black triangles: Root mean square deviation.

region is a photonic crystal in the x -direction, and band gaps are therefore expected for select frequency regions. The effect of both these considerations were tested by calculating a refractive index based on the method presented in Ref. [40]. Using this method the effect of propagation at an angle with respect to the x -axis in the layer was also tested. However, it was found that it had little effect, hence to preserve the computational speed the geometric average was chosen instead.

To test the validity of the PMM it is compared to the results obtained using the FMM model. To do this, the effective refractive index is first calculated for the photonic crystal layer of the structure. Based on this refractive index, the propagation constants are calculated for a slab waveguide of equal thickness, h , to that of the structure, for both S- and P-polarised light, after which the propagation constants, β_n , of any mode can be matched to any $k_{x,m}$ in accordance with Eq. 5. The intersections of these correspond to frequencies where a discrete and continuous set of modes are accessible, for which Fano resonances are expected. The procedure is illustrated in the second insert of Fig. 5, where the circles and triangles denote frequencies for which Fano resonances are expected for S- and P-polarised light, respectively. Fig. 6 shows the result of using the PMM and the FMM on a structure with the same parameters as the structure fabricated in this article. The location of the resonances predicted with PMM are denoted by triangles plotted at the same height as the resonances, asterisks, found from visual inspection of the FMM. Furthermore to condense and quantify the data, boxplots has also been made over the differences in the placement of the resonances between the PMM and FMM, calculated from Eq. 6,

$$\Delta\nu = \nu_{PMM} - \nu_{FMM}. \quad (6)$$

In a box plot, a box of arbitrary width contains the second and third quartile of the data set, separated by the median value, marked with a horizontal line. Each quartile contains a quarter

of the data points. At the bottom and top of the box a dashed line goes to the minimum and maximum of the data set, marked with horizontal lines, containing the first and fourth quartile, respectively. The number of Fano resonances are shown over each box plot, and the root-mean-square-difference (RMSD) between the two models are also calculated, marked with a triangle. Generally it can be seen that there is great agreement between the two models, though slightly better for the S-polarisation. Half of the resonances found with PMM are within ~ 13 GHz of those found using FMM, while the entire data set is within 55 GHz. The RMSD are 9.7 and 15.4 GHz for S- and P- polarisation respectively. Besides the advantage of reduced computational speed the PMM also find the resonance location without having to sort out other local minima that may appear in the spectrum. Furthermore, the frequency resolution of the PMM need not be as strict as the FMM to find the very narrow Fano resonances, such as the one located around 1.8 THz for the S-polarisation in Fig. 6. Hence the PMM presents advantages over the rigorous FMM while still showing great agreement.

5. Comparison of FMM and PMM

To further confirm the validity of the model a more quantitative analysis of the PMM is conducted. In this comparison the correspondence between the PMM and the FMM was analysed by examining the 36 different possible settings from combinations of the following: $\varepsilon = \{3.4^2\}$, $\Lambda = \{100, 125\} \mu\text{m}$, $w_t = \{21, 54\} \mu\text{m}$, $t = \{9, 15, 22\} \mu\text{m}$, and $h = \{101, 149, 201\} \mu\text{m}$. The FMM spectra are calculated with a spectral resolution of 0.1 GHz, and the Fano resonances are then found by visual inspection of the calculated spectra. The deviation between each peak calculated by the PMM and FMM is found from Eq. 6. For each setting a box plot was made over the calculated deviations, and the result is presented in Fig. 7. The average of the RMSD values are 20.14 GHz for the S-polarisation and 13.72 GHz for P-polarisation. With the largest RMSD value being 62.42 and 31.37 for S- and P-polarisation, respectively. It can also be seen in Fig. 7 that the extremes for S-polarised radiation is -67.4 GHz (setting 21) and 161.7 GHz (setting 12), where for P-polarised radiation the extremes are -73.8 GHz (setting 30) and 50.1 GHz (setting 34). Furthermore, for the settings examined here, the average absolute median deviation for the S-polarisation is 4.38 GHz and 2.40 GHz for the P-polarisation. If these values are compared with the box plot shown in Fig. 6 it can be seen that the general agreement shown in this figure is not an isolated incidence. In fact the plot shown in Fig. 6 represents the standard prediction accuracy of the PMM as the RMSD for this setting is close to the middle of the range of RMSD calculated for the 36 settings, as can be seen in Fig. 7. Hence, it is expected that the PMM will show just as good agreement for a wide range of settings as was the case for the fabricated sample shown in Fig. 6, despite the numerous approximations.

To determine the location of the Fano resonances a visual inspection was conducted of the FMM calculated transmission spectra. The FMM calculations were only done within the frequency range described in section 4, while the PMM was calculated 20% past the upper limit, to ensure resonances found with FMM right at the upper limit could always be matched with a prediction made by the PMM. Hence if multiple peaks were found in this extended region only the closest one were retained.

It is worth noting that besides the 1387 Fano Resonances found there are possible two additional resonances. For both cases the extra resonance either predicted by the PMM or found from the visual inspection of the FMM, was excluded. Common for both, and the reasoning for the exclusion, being that the modelled transmittance spectra were difficult to interpret around the discrepancies. Hence the number of peaks is predicted with very high accuracy with the PMM.

Fig. 7 also shows the great agreement between the PMM and the rigorous FMM as the observed trend is that for the majority of the settings the median is found rather close to zero deviation in the entire range of data points. Generally it is also observed that the spread of the two first quartiles is small compared to the spread of the whole data set. Hence the average RMSD

is also much lower than the extremes of the data set which shows that the general accuracy is high. The precision of the PMM is furthermore well within the prediction accuracy of other reported models, namely the 3D FEM model presented in Ref. [25], which shows a precision of prediction in the same range, i.e., within 59 and 98 GHz for S- and P-polarisation respectively. Given the correspondence between the model and the visual inspection presented above and in Fig. 7, we consider this model to be useful and reliable, when determining the placement of Fano resonances. The usefulness really comes in fruition as it is able to find very sharp peaks, which would otherwise require a high spectral resolution in the calculation as well as the reduced computational time.

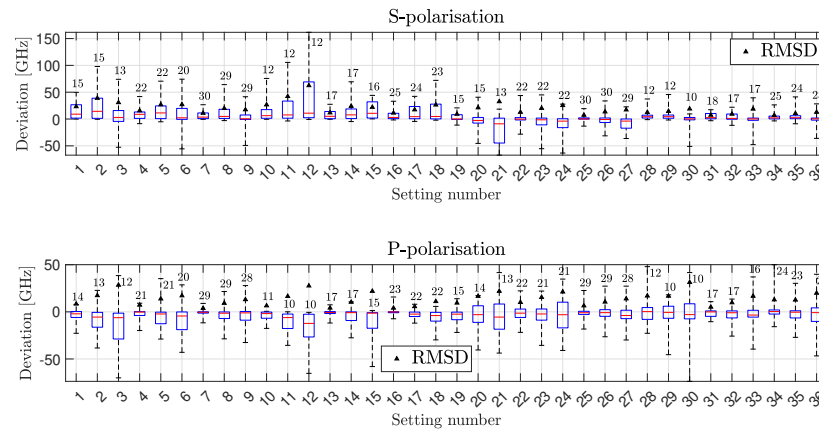


Fig. 7. Box plot of the deviation between the frequency locations of the Fano resonances from 36 dielectric structures for both polarisations. The average absolute median deviation for the S-polarisation is 4.38 GHz, and 2.40 GHz for the P-polarisation. The average RMSD is 20.14 and 13.72 GHz for the S- and P-polarisation, respectively.

6. Conclusion

We have studied transmission of THz radiation (0.8 – 2.4 THz) through an all-dielectric periodic sub-wavelength high-resistivity silicon grating and shown excellent agreement, ± 8 GHz, between measured and modelled Fano resonances for angles of incidence between 0° and 10° . Furthermore, a novel 1D propagation-constant-matching model was shown to predict the frequencies of resonances in excellent agreement with the Fourier Modal Method, having a root mean square deviation within 25 GHz for a wide range of modelled structures.

Acknowledgement. A special thanks to Mathias Hedegaard Kristensen who supplied a MATLAB program capable of performing the Fourier transforms.

Disclosures. The authors declare no conflicts of interest.

Data availability. Data underlying the results presented in this paper are available on request to the corresponding author.

References

1. A. G. Davies, A. D. Burnett, W. Fan, E. H. Linfield, and J. E. Cunningham, "Terahertz spectroscopy of explosives and drugs," *Mater. Today* **11**, 18–26 (2008).
2. J. F. Federici, B. Schulkin, F. Huang, D. Gary, R. Barat, F. Oliveira, and D. Zimdars, "THz imaging and sensing for security applications—explosives, weapons and drugs," *Semicond. Sci. Technol.* **20**, S266–S280 (2005).

- 254 3. S. S. Dhillon, M. S. Vitiello, E. H. Linfield, A. G. Davies, M. C. Hoffmann, J. Booske, C. Paoloni, M. Gensch,
255 P. Weightman, G. P. Williams, E. Castro-Camus, D. R. S. Cumming, F. Simoens, I. Escorcia-Carranza, J. Grant,
256 S. Lucyszyn, M. Kuwata-Gonokami, K. Konishi, M. Koch, C. A. Schmuttenmaer, T. L. Cocker, R. Huber, A. G.
257 Markelz, Z. D. Taylor, V. P. Wallace, J. A. Zeitler, J. Sibik, T. M. Korter, B. Ellison, S. Rea, P. Goldsmith, K. B.
258 Cooper, R. Appleby, D. Pardo, P. G. Huggard, V. Krozer, H. Shams, M. Fice, C. Renaud, A. Seeds, A. Stöhr,
259 M. Naftaly, N. Ridler, R. Clarke, J. E. Cunningham, and M. B. Johnston, "The 2017 terahertz science and technology
260 roadmap," *J. Phys. D: Appl. Phys.* **50**, 043001 (2017).
- 261 4. C. Jansen, S. Wietzke, O. Peters, M. Scheller, N. Vieweg, M. Salhi, N. Krumbholz, C. Jördens, T. Hochrein, and
262 M. Koch, "Terahertz imaging: applications and perspectives," *Appl. Opt.* **49**, E48–E57 (2010).
- 263 5. M. Tonouchi, "Cutting-edge terahertz technology," *Nat. Photonics* **1**, 97–105 (2007).
- 264 6. S. Wietzke, C. Jansen, N. Krumbholz, O. Peters, N. Vieweg, C. Jördens, M. Scheller, D. Romeike, T. Jung, M. Reuter,
265 S. Chatterjee, M. Koch, F. Physik, B. Baudrit, T. Zentgraf, T. Hochrein, and M. Bastian, "Terahertz spectroscopy: A
266 powerful tool for the characterization of plastic materials," in *2010 10th IEEE International Conference on Solid
267 Dielectrics*, (2010), pp. 1–4.
- 268 7. G. G. Hernandez-Cardoso, L. F. Amador-Medina, G. Gutierrez-Torres, E. S. Reyes-Reyes, C. A. Benavides Martínez,
269 C. Cardona Espinoza, J. Arce Cruz, I. Salas-Gutierrez, B. O. Murillo-Ortiz, and E. Castro-Camus, "Terahertz imaging
270 demonstrates its diagnostic potential and reveals a relationship between cutaneous dehydration and neuropathy for
271 diabetic foot syndrome patients," *Sci. Reports* **12**, 3110 (2022).
- 272 8. I. V. Il'ina, D. S. Sitnikov, and M. B. Agranat, "State-of-the-art of studies of the effect of terahertz radiation on living
273 biological systems," *High Temp.* **56**, 789–810 (2018).
- 274 9. B. Ferguson and X.-C. Zhang, "Materials for terahertz science and technology," *Nat. Mater.* **1**, 26–33 (2002).
- 275 10. H. Viswanathan and P. E. Mogensen, "Communications in the 6g era," *IEEE Access* **8**, 57063–57074 (2020).
- 276 11. S. Dang, O. Amin, B. Shihada, and M.-S. Alouini, "What should 6g be?" *Nat. Electron.* **3**, 20–29 (2020).
- 277 12. C. Xu, Z. Ren, J. Wei, and C. Lee, "Reconfigurable terahertz metamaterials: From fundamental principles to advanced
278 6g applications," *iScience* **25**, 103799 (2022).
- 279 13. A. Kaur, J. C. Myers, M. I. M. Ghazali, J. Byford, and P. Chahal, "Affordable terahertz components using 3d printing,"
280 in *2015 IEEE 65th Electronic Components and Technology Conference (ECTC)*, (2015), pp. 2071–2076.
- 281 14. X. Cui, H. Tian, Y. Du, G. Shi, and Z. Zhou, "Normal incidence filters using symmetry-protected modes in dielectric
282 subwavelength gratings," *Sci. Reports* **6**, 36066 (2016).
- 283 15. M. F. Limonov, M. V. Rybin, A. N. Poddubny, and Y. S. Kivshar, "Fano resonances in photonics," *Nat. Photonics* **11**,
284 543–554 (2017).
- 285 16. Q. Xie, G.-X. Dong, B.-X. Wang, and W.-Q. Huang, "High-q fano resonance in terahertz frequency based on an
286 asymmetric metamaterial resonator," *Nanoscale Res. Lett.* **13**, 294 (2018).
- 287 17. C. Wu, N. Arju, G. Kelp, J. A. Fan, J. Dominguez, E. Gonzales, E. Tutuc, I. Brener, and G. Shvets, "Spectrally
288 selective chiral silicon metasurfaces based on infrared fano resonances," *Nat. Commun.* **5**, 3892 (2014).
- 289 18. R. Singh, I. A. I. Al-Naib, M. Koch, and W. Zhang, "Sharp fano resonances in thz metamaterials," *Opt. Express* **19**,
290 6312–6319 (2011).
- 291 19. Y. Wang, S. Jia, and J. Qin, "Tunable fano resonance and enhanced sensing in terahertz metamaterial," *Front. Phys.* **8**
292 (2021).
- 293 20. X. Romain, R. Degl'Innocenti, F. I. Baida, and P. Boyer, "Tunable polarization-induced fano resonances in stacked
294 wire-grid metasurfaces," *Commun. Phys.* **4**, 115 (2021).
- 295 21. Y. P. Cao, Y. Y. Wang, Z. X. Geng, J. Liu, Y. P. Yang, and H. D. Chen, "Tuning of fano resonances in terahertz
296 metamaterials," *J. Appl. Phys.* **117**, 063107 (2015).
- 297 22. Z. Liu, Z. Liu, J. Li, W. Li, J. Li, C. Gu, and Z.-Y. Li, "3d conductive coupling for efficient generation of prominent
298 fano resonances in metamaterials," *Sci. Reports* **6**, 27817 (2016).
- 299 23. U. Fano, "Effects of configuration interaction on intensities and phase shifts," *Phys. Rev.* **124**, 1866–1878 (1961).
- 300 24. A. A. Darki, A. Parthenopoulos, J. V. Nygaard, and A. Dantan, "Profilometry and stress analysis of suspended
301 nanostructured thin films," *J. Appl. Phys.* **129**, 065302 (2021).
- 302 25. Y. Yang, B. Cui, Z. Geng, and S. Feng, "Terahertz magnetic and electric mie resonances of an all-dielectric
303 one-dimensional grating," *Appl. Phys. Lett.* **106**, 111106 (2015).
- 304 26. Y. Shuai, D. Zhao, Z. Tian, J.-H. Seo, D. V. Plant, Z. Ma, S. Fan, and W. Zhou, "Double-layer fano resonance
305 photonic crystal filters," *Opt. Express* **21**, 24582–24589 (2013).
- 306 27. Y. Wang, D. Stellinga, A. B. Klemm, C. P. Reardon, and T. F. Krauss, "Tunable optical filters based on silicon nitride
307 high contrast gratings," *IEEE J. Sel. Top. Quantum Electron.* **21**, 108–113 (2015).
- 308 28. F. Brückner, D. Friedrich, T. Clausnitzer, M. Britzger, O. Burmeister, K. Danzmann, E.-B. Kley, A. Tünnermann, and
309 R. Schnabel, "Realization of a monolithic high-reflectivity cavity mirror from a single silicon crystal," *Phys. Rev.
310 Lett.* **104**, 163903 (2010).
- 311 29. X. Gao, T. Wu, Y. Xu, X. Li, D. Bai, G. Zhu, H. Zhu, and Y. Wang, "Angular-dependent polarization-insensitive filter
312 fashioned with zero-contrast grating," *Opt. Express* **23**, 15235–15241 (2015).
- 313 30. M. Niraula, J. W. Yoon, and R. Magnusson, "Concurrent spatial and spectral filtering by resonant nanogratings," *Opt.
314 Express* **23**, 23428–23435 (2015).
- 315 31. A. Parthenopoulos, A. A. Darki, B. R. Jeppesen, and A. Dantan, "Optical spatial differentiation with suspended
316 subwavelength gratings," *Opt. Express* **29**, 6481–6494 (2021).

- 317 32. N. Gregersen, "Fourier Modal Method," in *Numerical Methods in Photonics*, (CRC Press, 2017), Optical Sciences
318 and Applications of Light, chap. 6, pp. 139–194, 1st ed.
- 319 33. B. Bhushan, *Springer Handbook of Nanotechnology*, Springer Handbook of Nanotechnology (Springer Berlin
320 Heidelberg, 2010).
- 321 34. M. Shearn, X. Sun, M. D. Henry, A. Yariv, and A. Scherer, "Advanced plasma processing: Etching, deposition, and
322 wafer bonding techniques for semiconductor applications," in *Semiconductor Technologies*, J. Grym, ed. (IntechOpen,
323 Rijeka, 2010), chap. 5.
- 324 35. M. Tilli, M. Paulasto-Krockel, M. Petzold, H. Theuss, T. Motooka, and V. Lindroos, *Handbook of silicon based*
325 *MEMS materials and technologies* (Elsevier, 2020).
- 326 36. H. F. Winters and J. Coburn, "Surface science aspects of etching reactions," *Surf. Sci. Reports* **14**, 162–269 (1992).
- 327 37. P. P. Cielecki and E. Skovsen, "A Compact, 3D printable Purge System for Terahertz Spectroscopy," (2021).
- 328 38. P. U. Jepsen, "Phase retrieval in terahertz time-domain measurements: a "how to" tutorial," *J. Infrared, Millimeter,*
329 *Terahertz Waves* **40**, 395–411 (2019).
- 330 39. J. D. Joannopoulos, S. G. Johnson, J. N. Winn, and R. D. Meade, *Photonic Crystals: Molding the Flow of Light*
331 (Princeton University Press, 2008), 2nd ed.
- 332 40. M. Centini, C. Sibilía, M. Scalora, G. D'Aguanno, M. Bertolotti, M. J. Bloemer, C. M. Bowden, and I. Nefedov,
333 "Dispersive properties of finite, one-dimensional photonic band gap structures: Applications to nonlinear quadratic
334 interactions," *Phys. Rev. E* **60**, 4891–4898 (1999).